Lu, X.; Blawert, C.; Kainer, K.U.; Zhang, T.; Wang, F.; Zheludkevich, M.L.:
Influence of particle additions on corrosion and wear resistance of plasma electrolytic oxidation coatings on Mg alloy.
In: Surface and Coatings Technology. Vol. 352 (2018) 1 - 14.
First published online by Elsevier: August 02, 2018

DOI: 10.1016/j.surfcoat.2018.08.003
https://dx.doi.org/10.1016/j.surfcoat.2018.08.003

Influence of particle additions on corrosion and wear resistance of plasma electrolytic oxidation coatings on Mg alloy

Xiaopeng Lu [a,b]*, Carsten Blawert [b], Karl Ulrich Kainer [b], Tao Zhang [a], Fuhui Wang [a], Mikhail L. Zheludkevich [b,c]

[a] *Corrosion and Protection Division, Shenyang National Laboratory for Materials Science, Northeastern University, 3-11 Wenhua Road, Shenyang 110819, China*

[b] *MagIC – Magnesium Innovation Centre, Institute of Materials Research, Helmholtz-Zentrum Geesthacht, Max-Planck-Str. 1, 21502 Geesthacht, Germany*

[c] *Faculty of Engineering, University of Kiel, Kaiserstrasse 2, 24143 Kiel, Germany*

**Corresponding author: Dr. Xiaopeng Lu (luxiaopeng@mail.neu.edu.cn)*

Abstract

The influence of particles with different melting points on the microstructure, phase composition and properties of plasma electrolytic oxidation (PEO) coatings was investigated. PEO coatings were produced on AM50 Mg alloy from an alkaline phosphate-based electrolyte (1 g/L KOH + 20 g/L Na_3PO_4) with and without addition of clay, SiO_2, Si_3Ni_4 and SiC micro-sized particles. The incorporation mode of the particles primarily depends on their melting point. Particles with relatively low melting point can achieve fully reactive incorporation, while high melting point particles are mainly inertly incorporated into the coating. Reactive incorporation of clay particles contributes to formation of a dense layer and improvement of corrosion and wear resistance. Addition of SiO_2 and Si_3Ni_4 particles can improve the wear resistance of PEO coating, while the corrosion performance and degradation process of the coating is marginally influenced by the inertly incorporated particles.

1. Introduction

Magnesium (Mg) alloys are of great potential to be utilized in aerospace, automotive industry and biomedical application due to low density, high specific strength and excellent machinability [1-5]. However, poor corrosion resistance and high chemical reactivity are the main obstacles

that impede the wide range of applications for Mg alloys [6-10]. Plasma electrolytic oxidation (PEO) is a promising surface treatment process derived from conventional anodizing to form ceramic-like coatings on light metal and its alloys, which is used for corrosion and wear protection [11-16]. The coatings are formed under high voltage which generates short-lived discharges on the metal surface resulting in a high pressure and temperature environment [17-20]. Regarding Mg and its alloys, a two- or three-layer structure is typically observed with a characteristic thin barrier layer laying directly on the metal surface, of a few hundred nanometers thickness, and an outer porous layer which is the main issue to achieve long-term protection [21-24]. Introduction of particles to the PEO electrolyte has been explored as a new strategy to seal the open pores and to provide a wider range of phase composition for PEO coatings [25-31]. Lee et al. [32] have added TiO_2 and ZrO_2 particles to a phosphate electrolyte to fabricate PEO coatings. It was found that the low melting point particles (TiO_2) were scarce in the layer while relatively high melting point particles (ZrO_2) were detectable in the coating. Our previous study proved that clay particles were melted and reactively incorporated into the coating due to the relatively low melting point [33, 34]. The particles can be considered as sintering additives to lower the sintering temperature during coating growth process, leading to formation of pure amorphous phase. Meanwhile the high-intensity discharges and high energy input applied during PEO process are capable of melting the inert particles and formation of new phase composition for the coating [35]. Therefore, the melting point of the particles is one of the key factors to determine the incorporation mode, i.e., reactive or inert incorporation into PEO coating, which will in turn influence the microstructure, phase composition and properties of the coating. However, there are only limited number of reports on the effect of particles with different melting points on PEO coated Mg alloy [31, 32, 36]. In the present study, micro-sized clay, SiO_2,

Si_3Ni_4 and SiC particles have been selected to investigate the addition of particles on the corrosion and wear performance of PEO coatings.

2. Experimental

Specimens of AM50 Mg alloy with size of 15 mm × 15 mm × 4 mm were prepared from gravity cast ingot material. The chemical composition (4.74% Al, 0.383% Mn, 0.065% Zn, 0.063% Si, 0.002% Fe, 0.002% Cu and Mg balance) of the alloy was measured by an Arc Spark OES (Spark analyser M9, Spectro Ametek, Germany). The specimens were ground using emery papers up to 1200 grit and then air-dried prior to PEO treatment. The PEO process was carried out by using a pulsed DC power source with a pulse ratio of t_{on}: t_{off} = 0.4 ms: 3.6 ms. The specimen and a stainless steel tube were used as the anode and cathode, respectively. It is more practical to find similar micro-sized particles and to trace the relatively large-sized particles in the coating compared to the nano-sized particles. Therefore, particles (5 g/L) with different melting points were selected for PEO treatment, i.e., clay (Rockwood Nanofil® 116, $(Na,Ca)_{0.33}(Al,Mg)_2(Si_4O_{10})(OH)_2 \cdot nH_2O$, <1200 C, ~12 μm), SiO_2 (1600 C, 1-5 μm), Si_3N_4 (1900 C, 1-5 μm) and SiC (2730 C, 1-5 μm), as shown in Fig. 1. A stirrer and bubbling generator were used to facilitate the uniform distribution of the particles in the electrolyte. To trace the particles, phosphate-based electrolyte was used (1 g/L KOH and 20 g/L Na_3PO_4). The corresponding coatings are named as PPEO, PPEO (clay), PPEO (SiO_2), PPEO (Si_3N_4) and PPEO (SiC), respectively. All the PEO treatments were performed at a constant voltage of 450 V for 10 min and the average current density provided by the DC power supply was limited to 300 mA/cm^2. Surface roughness measurements were carried out with a Hommel profilometer (HOMMEL TESTER T1000). A scanning electron microscope (TESCAN Vega3 SB) combined with an energy dispersive spectrometer (EDS) system from eumeX (ixrfsystems) was used to

examine the morphology and composition of the coatings. The phase composition of the coatings was measured by a Bruker X-ray diffractometer using Cu Kα radiation.

The corrosion behavior of the PEO coatings was assessed by potentiodynamic polarization and electrochemical impedance spectroscopy (EIS) tests, which were carried out using an ACM Gill AC computer controlled potentiostat. A typical three-electrode cell with the coated specimen as the working electrode (0.5 cm^2 exposed area), a saturated Ag/AgCl electrode as the reference electrode, and a platinum mesh as counter electrode was used. Polarization investigations were carried out starting at -150 mV relative to OCP (after 30 min of exposure at OCP) at a sweep rate of 0.2 mV s^{-1} until the anodic branch reached a final current density of 0.01 $mA.cm^{-2}$. Electrochemical impedance spectroscopy (EIS) studies were performed at open circuit potential with AC amplitude of 10 mV RMS sinusoidal perturbations over the frequency range from 30 kHz to 0.01 Hz. The measurements were repeated at fixed intervals of 0 (after 5 min immersion), 1, 3, 6, 12, 24, 48 and 72 h of immersion time. The dry sliding wear behavior of the PEO coatings was assessed with a Tribotec ball-on-disc oscillating tribometer with an AISI 52100 steel ball of 6 mm diameter as static friction partner. The wear tests were performed at ambient conditions (25 ± 2 °C and 30 % R.H.) under 1, 3 and 5 N load with oscillating amplitude of 10 mm and at a sliding velocity of 5 mm s^{-1} for a sliding distance of 12 m.

3. Results and discussion

3.1. Microstructure, phase and elemental composition of the coatings

The surface morphology of the PEO coatings is shown in Fig. 2. The coating surface has not been influenced greatly by the particles, except that some tiny particles can be found for all coatings produced from particle containing electrolytes. The roughness of the coatings in the

presence of particles is slightly higher than that of the particle free coating, for instance, 3.0 ± 0.3 µm for PPEO (clay), 3.1 ± 0.2 µm for PPEO (SiO_2), 3.3 ± 0.1 µm for PPEO (Si_3N_4), 3.6 ± 0.4 µm for PPEO (SiC) in comparison to 2.8 ± 0.3 µm for PPEO. Fig. 3 exhibits the cross section of the coatings. It is obvious that the growth rate of the coating has been reduced after incorporation of particles, since the particle-free coating is the thickest (45 ± 5 µm) among all the coatings. The coating (26 ± 5 µm) with addition of clay particles is thinner than the other coatings, namely, 33 ± 4 µm for PPEO (SiO_2), 35 ± 8 µm for PPEO (Si_3N_4) and 33 ± 5 µm for PPEO (SiC).

The element and phase composition of the coatings are shown in Fig. 4. According to the EDS analysis (Fig. 4a), the content of the main elements (O, Mg and P) of the coating is similar. The detection of Si indicates that all the particles have participated in the coating formation process and are incorporated into the layer. However, the incorporated amount of the particles is different for various coatings. The particle content (12 at. % Si) of PPEO (SiC) is the maximum among all the coatings. The Si content (6 at. %) of PPEO (SiO_2) is slightly higher than that of PPEO (clay) (5.4 at. %) and PPEO (Si_3N_4) (5 at. %). It can be inferred that the uptake of particles is related with the number and size of the pores, since PPEO (SiC) is more porous compared to the other coatings. In terms of coating phase composition (Fig. 4b), a large broad bump with 2θ angle distributed over 20°-35° is visible for all the coatings, which has been confirmed as phosphate containing amorphous phase [33, 37]. Apart from that, small amount of MgO is detected in the layer except PPEO (clay). It is worth to note that SiO_2, Si_3N_4 and SiC particles are found in the coating, while clay particles are not observed after PEO treatment. Therefore, low melting point particles (clay particles) demonstrate fully reactive incorporation and particles with relatively high melting point are mainly inertly incorporated into the coating, indicating that the melting point of the particles influences its incorporation mode under certain energy input.

To further confirm the incorporation of particles into PEO coating, EDS mapping analysis was performed to identify the particle distribution (Fig. 5). The main elements (O, Mg and P) are uniformly distributed across the whole layer. The Si distribution is different among the coatings, as the Si signal of PPEO (clay) is much more homogenous in comparison to that of the other coatings. Therefore, the micro-sized SiO_2, Si_3N_4 and SiC particles are primarily inertly incorporated into the layer, while clay particles have been melted resulting in an amorphous coating. Our previous studies have proved that the size of the particles plays an important role in the incorporation mode [37, 38]. Besides the size, the melting point of the particles is also crucial to the incorporation mode of the particles and phase composition of the coating. The reactive incorporation of clay particles verifies that low melting point particles are capable of being melted by the short-lived discharges and subsequently react with other components, while high melting point particles are hardly to be melted and transformed to new phases.

3.2. Corrosion performance

The corrosion resistance of PEO coatings was evaluated by potentiodynamic polarization (Fig. 6). The corrosion potential (E_{corr}), corrosion current density (i_{corr}) and breakdown potential (E_{bd}) derived from the polarization plots are summarized in Table 1. It is apparent that the corrosion current density ($(8.7 \pm 2.2) \times 10^{-6}$ mA.cm^{-2}) of the coating loaded with clay particles are much lower than that of the other coatings. The current density of coatings with SiO_2, Si_3N_4 and SiC addition is slightly higher than that of particle free coating, i.e., $(1.2 \pm 0.2) \times 10^{-4}$ mA.cm^{-2} for PPEO, $(1.9 \pm 0.7) \times 10^{-4}$ mA.cm^{-2} for PPEO (SiO_2), $(1.8 \pm 0.5) \times 10^{-4}$ mA.cm^{-2} for PPEO (Si_3N_4) and $(2 \pm 0.3) \times 10^{-4}$ mA.cm^{-2} for PPEO (SiC), respectively. There is nearly no effect on the corrosion potential of PEO coating after incorporation of SiO_2, Si_3N_4 and SiC particles, since the corrosion potential is almost equal (from -1552 ± 7 mV to -1588 ± 10 mV). However, the

coating in the presence of clay particles demonstrates relatively negative corrosion potential compared to other coatings, which might be ascribed to the surface condition of the exposed substrate and the environment in the pores. In addition, the breakdown potential (-1398 ± 8 mV) of PPEO (clay) is slightly higher compared to that of the other coatings (from -1433 ± 6 mV to -1466 ± 17 mV). Note that polarization test only provides limited information and reflects the short-term corrosion resistance of the layer, and thus long-term EIS measurements have been performed to determine the corrosion performance of the PEO coatings. The EIS spectra (Bode plots) of the coatings are presented in Fig. 7. It can be seen that all the coatings degrade continually as a function of the immersion time. Two well-defined time constants can be detected in all Bode plots at low (1 Hz) and high (10^4 Hz) frequency for the first measurement, which was performed after immersion for 5 min. The coatings start to degrade afterwards due to the penetration of the corrosive Cl^- ions through the open pores/defects in the outer layer. Therefore, the contribution of the outer porous layer to the high frequency impedance is weakened, leading to a merged time constant with the low frequency which stands for the inner layer. Meanwhile the corrosion process occurs at the metal/electrolyte interface with a sign of an additional time constant at the low frequency range (0.01-0.1 Hz). The time constant related to the outer layer disappears with further increase of immersion time. The impedance at the lowest frequency (0.01 Hz) is used to represent the total corrosion resistance of the coating (Fig. 8) [37, 39, 40]. The initial corrosion resistance of particle-containing coatings is higher than that of the blank coating. The corrosion resistance of PPEO (clay) is slightly higher in comparison to that of the other coatings during the whole corrosion test, which is consistent with the polarization measurements. The reactive incorporation of particles facilitates formation of a dense layer, leading to the improvement of the corrosion resistance. However, the degradation process of the

coating is not influenced by the incorporated particles. Future work could be focused on the incorporation of inhibitor-containing nanocontainers into PEO coating to provide active corrosion protection for Mg surface.

3.3. Tribological performance

The wear tracks of the PEO coatings against a steel ball under 1 N load are shown in Fig. 9. The surface of all the coatings is covered by wear debris, among which the wear track of PPEO (clay) and PPEO (SiO_2) appears to be more intact and the original coating is still visible without severe damage. In terms of the wear track under 3 N (Fig. 10), the width and volume of the wear track increase greatly and the original coating is hardly to be found. Besides, many cracks can be seen in the wear track. With the load further increase to 5 N (Fig. 11), the wear tracks become bigger and larger than that of the coating tested under lower load. Especially for PPEO and PPEO (SiC), the substrate is exposed and the coating has been removed completely. Fig. 12a shows the wear rate of the coatings under various loads. It is obvious that incorporation of particles could improve the wear resistance of the coating, specifically for the coating loaded with clay and SiO_2 particles. Due to the similar tendency under low loads (1 N and 3 N), the variation of the friction coefficient during the wear test under load of 5 N is shown in Fig. 12b. In the case of the coating without and with SiC particles, the friction coefficient rises from 0.12 to around 0.78 within a relatively short period, which is followed by sharp fluctuations, suggesting a failure of the coating. In contrast, the friction coefficient of the coatings with addition of clay, SiO_2 and Si_3N_4 particles increases from 0.12 to a steady-state value of 0.7 ± 0.1 during 2 m and 12 m of sliding. The enhancement of the wear resistance of the coating can be attributed to the newly formed amorphous phase (reactive incorporation) and the inertly incorporated particles, leading to a dense layer and/or high coating hardness. However, the wear performance of the coating can be

deteriorated when the layer becomes porous and defective with excessive amount of inertly incorporated particles.

4. Conclusions

1) The incorporation mode of the introduced micro-sized particles mainly depends on their melting point under certain energy input, i.e., reactive incorporation for low melting point particles and inert incorporation for high melting point particles.

2) Reactive incorporation of clay particles contributes to formation of a dense layer and thus improves the corrosion and wear resistance of the coating.

3) The wear resistance of PEO coating has been improved by the inertly incorporated SiO_2 and Si_3N_4 particles, while the degradation process remains unchanged since the microstructure and main phase composition of the layer is not modified in the presence of particles. Incorporation of excessive amount of SiC particles is detrimental to the corrosion and wear property of the coating.

Acknowledgements

The technical support of Mr. Volker Heitmann and Mr. Ulrich Burmester during this work is gratefully acknowledged. The authors would like to acknowledge the financial support of the National Natural Science Foundation of China (NO. U1737102, 51531007 and 51771050), Young Elite Scientists Sponsorship Program by China Association for Science and Technology (2017QNRC001), and Fundamental Research Funds for the Central Universities (N170203006 and N170205002).

Reference

[1] N.V. Phuong, K.H. Lee, D. Chang, S. Moon, Effects of Zn2+ concentration and pH on the zinc phosphate conversion coatings on AZ31 magnesium alloy, Corrosion Science, 74 (2013) 314-322.
[2] Y.C. Su, Y.C. Su, Y.B. Lu, J.S. Lian, G.Y. Li, Composite Microstructure and Formation Mechanism of Calcium Phosphate Conversion Coating on Magnesium Alloy, J Electrochem Soc, 163 (2016) G138-G143.
[3] M. Esmaily, J.E. Svensson, S. Fajardo, N. Birbilis, G.S. Frankel, S. Virtanen, R. Arrabal, S. Thomas, L.G. Johansson, Fundamentals and advances in magnesium alloy corrosion, Progress in Materials Science, 89 (2017) 92-193.
[4] G. Duan, L. Yang, S. Liao, C. Zhang, X. Lu, Y. Yang, B. Zhang, Y. Wei, T. Zhang, B. Yu, X. Zhang, F. Wang, Designing for the chemical conversion coating with high corrosion resistance and low electrical contact resistance on AZ91D magnesium alloy, Corrosion Science, 135 (2018) 197-206.
[5] Z.-H. Xie, S. Shan, Nanocontainers-enhanced self-healing Ni coating for corrosion protection of Mg alloy, Journal of Materials Science, 53 (2018) 3744-3755.
[6] J. Song, F. Pan, B. Jiang, A. Atrens, M.-X. Zhang, Y. Lu, A review on hot tearing of magnesium alloys, Journal of Magnesium and Alloys, 4 (2016) 151-172.
[7] L. Yang, G. Liu, L. Ma, E. Zhang, X. Zhou, G. Thompson, Effect of iron content on the corrosion of pure magnesium: Critical factor for iron tolerance limit, Corrosion Science, 139 (2018) 421-429.
[8] L. Wu, D. Yang, G. Zhang, Z. Zhang, S. Zhang, A. Tang, F. Pan, Fabrication and characterization of Mg-M layered double hydroxide films on anodized magnesium alloy AZ31, Applied Surface Science, 431 (2018) 177-186.
[9] X. Wang, L. Li, Z.-H. Xie, G. Yu, Duplex coating combining layered double hydroxide and 8-quinolinol layers on Mg alloy for corrosion protection, Electrochimica Acta, 283 (2018) 1845-1857.
[10] X. Lu, Y. Chen, C. Zhang, T. Zhang, B. Yu, H. Xu, F. Wang, Formation Mechanism and Corrosion Performance of Phosphate Conversion Coatings on AZ91 and Mg-Gd-Y-Zr Alloy, J Electrochem Soc, 165 (2018) C601-C607.
[11] J.A. Curran, T.W. Clyne, Thermo-physical properties of plasma electrolytic oxide coatings on aluminium, Surface and Coatings Technology, 199 (2005) 168-176.
[12] R. Arrabal, E. Matykina, T. Hashimoto, P. Skeldon, G.E. Thompson, Characterization of AC PEO coatings on magnesium alloys, Surface and Coatings Technology, 203 (2009) 2207-2220.
[13] Y. Song, K. Dong, D. Shan, E.-H. Han, Investigation of a novel self-sealing pore micro-arc oxidation film on AM60 magnesium alloy, Journal of Magnesium and Alloys, 1 (2013) 82-87.
[14] X. Lu, M. Mohedano, C. Blawert, E. Matykina, R. Arrabal, K.U. Kainer, M.L. Zheludkevich, Plasma electrolytic oxidation coatings with particle additions – A review, Surface and Coatings Technology, 307, Part C (2016) 1165-1182.
[15] P.H. Sobrinho, Y. Savguira, Q. Ni, S.J. Thorpe, Statistical analysis of the voltage-time response produced during PEO coating of AZ31B magnesium alloy, Surface and Coatings Technology, 315 (2017) 530-545.
[16] J. Yang, C. Blawert, S.V. Lamaka, D. Snihirova, X. Lu, S. Di, M.L. Zheludkevich, Corrosion protection properties of inhibitor containing hybrid PEO-epoxy coating on magnesium, Corrosion Science, 140 (2018) 99-110.
[17] S. Moon, R. Arrabal, E. Matykina, 3-Dimensional structures of open-pores in PEO films on AZ31 Mg alloy, Materials Letters, 161 (2015) 439-441.
[18] M. Daroonparvar, M.A.M. Yajid, N.M. Yusof, H.R. Bakhsheshi-Rad, Preparation and corrosion resistance of a nanocomposite plasma electrolytic oxidation coating on Mg-1%Ca alloy formed in aluminate electrolyte containing titania nano-additives, Journal of Alloys and Compounds, 688, Part A (2016) 841-857.
[19] S. Stojadinović, N. Tadić, N. Radić, B. Grbić, R. Vasilić, MgO/ZnO coatings formed on magnesium alloy AZ31 by plasma electrolytic oxidation: Structural, photoluminescence and photocatalytic investigation, Surface and Coatings Technology, 310 (2017) 98-105.

[20] X. Lu, C. Blawert, D. Tolnai, T. Subroto, K.U. Kainer, T. Zhang, F. Wang, M.L. Zheludkevich, 3D reconstruction of plasma electrolytic oxidation coatings on Mg alloy via synchrotron radiation tomography, Corrosion Science, 139 (2018) 395-402.
[21] L. Yu, J. Cao, Y. Cheng, An improvement of the wear and corrosion resistances of AZ31 magnesium alloy by plasma electrolytic oxidation in a silicate–hexametaphosphate electrolyte with the suspension of SiC nanoparticles, Surface and Coatings Technology, 276 (2015) 266-278.
[22] K. Dong, Y. Song, D. Shan, E.-H. Han, Corrosion behavior of a self-sealing pore micro-arc oxidation film on AM60 magnesium alloy, Corrosion Science, 100 (2015) 275-283.
[23] L.-Y. Cui, H.-P. Liu, W.-L. Zhang, Z.-Z. Han, M.-X. Deng, R.-C. Zeng, S.-Q. Li, Z.-L. Wang, Corrosion resistance of a superhydrophobic micro-arc oxidation coating on Mg-4Li-1Ca alloy, Journal of Materials Science & Technology, (2017).
[24] S. Stojadinović, R. Vasilić, J. Radić-Perić, M. Perić, Characterization of plasma electrolytic oxidation of magnesium alloy AZ31 in alkaline solution containing fluoride, Surface and Coatings Technology, 273 (2015) 1-11.
[25] D. Zhang, Y. Gou, Y. Liu, X. Guo, A composite anodizing coating containing superfine Al2O3 particles on AZ31 magnesium alloy, Surface and Coatings Technology, 236 (2013) 52-57.
[26] M. Mohedano, C. Blawert, M.L. Zheludkevich, Silicate-based Plasma Electrolytic Oxidation (PEO) coatings with incorporated CeO2 particles on AM50 magnesium alloy, Materials & Design, 86 (2015) 735-744.
[27] B.-S. Lou, Y.-Y. Lin, C.-M. Tseng, Y.-C. Lu, J.-G. Duh, J.-W. Lee, Plasma electrolytic oxidation coatings on AZ31 magnesium alloys with Si3N4 nanoparticle additives, Surface and Coatings Technology, 332 (2017) 358-367.
[28] D.V. Mashtalyar, S.V. Gnedenkov, S.L. Sinebryukhov, I.M. Imshinetskiy, A.V. Puz', Plasma electrolytic oxidation of the magnesium alloy MA8 in electrolytes containing TiN nanoparticles, Journal of Materials Science & Technology, 33 (2017) 461-468.
[29] J. Yang, X. Lu, C. Blawert, S. Di, M.L. Zheludkevich, Microstructure and corrosion behavior of Ca/P coatings prepared on magnesium by plasma electrolytic oxidation, Surface and Coatings Technology, 319 (2017) 359-369.
[30] Y. Chen, X. Lu, C. Blawert, M.L. Zheludkevich, T. Zhang, F. Wang, Formation of self-lubricating PEO coating via in-situ incorporation of PTFE particles, Surface and Coatings Technology, 337 (2018) 379-388.
[31] M. Mohedano, R. Arrabal, B. Mingo, A. Pardo, E. Matykina, Role of particle type and concentration on characteristics of PEO coatings on AM50 magnesium alloy, Surface and Coatings Technology, 334 (2018) 328-335.
[32] K.M. Lee, B.U. Lee, S.I. Yoon, E.S. Lee, B. Yoo, D.H. Shin, Evaluation of plasma temperature during plasma oxidation processing of AZ91 Mg alloy through analysis of the melting behavior of incorporated particles, Electrochimica Acta, 67 (2012) 6-11.
[33] C. Blawert, S.P. Sah, J. Liang, Y. Huang, D. Höche, Role of sintering and clay particle additions on coating formation during PEO processing of AM50 magnesium alloy, Surface and Coatings Technology, 213 (2012) 48-58.
[34] X. Lu, S.P. Sah, N. Scharnagl, M. Störmer, M. Starykevich, M. Mohedano, C. Blawert, M.L. Zheludkevich, K.U. Kainer, Degradation behavior of PEO coating on AM50 magnesium alloy produced from electrolytes with clay particle addition, Surface and Coatings Technology, 269 (2015) 155-169.
[35] X. Lu, C. Blawert, K.U. Kainer, M.L. Zheludkevich, Investigation of the formation mechanisms of plasma electrolytic oxidation coatings on Mg alloy AM50 using particles, Electrochimica Acta, 196 (2016) 680-691.
[36] G. Barati Darband, M. Aliofkhazraei, P. Hamghalam, N. Valizade, Plasma electrolytic oxidation of magnesium and its alloys: Mechanism, properties and applications, Journal of Magnesium and Alloys, 5 (2017) 74-132.

[37] X. Lu, C. Blawert, Y. Huang, H. Ovri, M.L. Zheludkevich, K.U. Kainer, Plasma electrolytic oxidation coatings on Mg alloy with addition of SiO2 particles, Electrochimica Acta, 187 (2016) 20-33.
[38] X. Lu, C. Blawert, M.L. Zheludkevich, K.U. Kainer, Insights into plasma electrolytic oxidation treatment with particle addition, Corrosion Science, 101 (2015) 201-207.
[39] S.V. Lamaka, M.F. Montemor, A.F. Galio, M.L. Zheludkevich, C. Trindade, L.F. Dick, M.G.S. Ferreira, Novel hybrid sol-gel coatings for corrosion protection of AZ31B magnesium alloy, Electrochimica Acta, 53 (2008) 4773-4783.
[40] B. Mingo, R. Arrabal, M. Mohedano, Y. Llamazares, E. Matykina, A. Yerokhin, A. Pardo, Influence of sealing post-treatments on the corrosion resistance of PEO coated AZ91 magnesium alloy, Applied Surface Science, 433 (2018) 653-667.

Figure captions

Fig. 1 Morphology and XRD patterns of the particles.

Fig. 2 Surface morphology of the coatings (a and b) PPEO, (c and d) PPEO (clay), (e and f) PPEO (SiO_2), (g and h) PPEO (Si_3N_4) and (i and j) PPEO (SiC).

Fig. 3 Cross section of the coatings (a) PPEO, (b) PPEO (clay), (c) PPEO (SiO_2), (d) PPEO (Si_3N_4) and (e) PPEO (SiC).

Fig. 4 (a) Surface composition determined by EDS, (b) XRD patterns of the coatings.

Fig. 5 Elemental distribution of the coatings with addition of particles (a) PPEO (clay), (b) PPEO (SiO_2), (c) PPEO (Si_3N_4) and (d) PPEO (SiC).

Fig. 6 Polarization curves of the coatings.

Fig. 7 Electrochemical impedance behavior of the PEO coatings (a) PPEO, (b) PPEO (clay), (c) PPEO (SiO_2), (d) PPEO (Si_3N_4) and (e) PPEO (SiC).

Fig. 8 Evolution of the impedance of the coatings at low frequency (0.01 Hz).

Fig. 9 Wear tracks of the PEO coatings against a steel ball under 1 N load.

Fig. 10 Wear tracks of the PEO coatings against a steel ball under 3 N load.

Fig. 11 Wear tracks of the PEO coatings against a steel ball under 5 N load.

Fig. 12 (a) Wear rate of the coatings under different loads and (b) variation of the friction coefficient during the 12 m sliding in the oscillating wear tests under a load of 5 N.

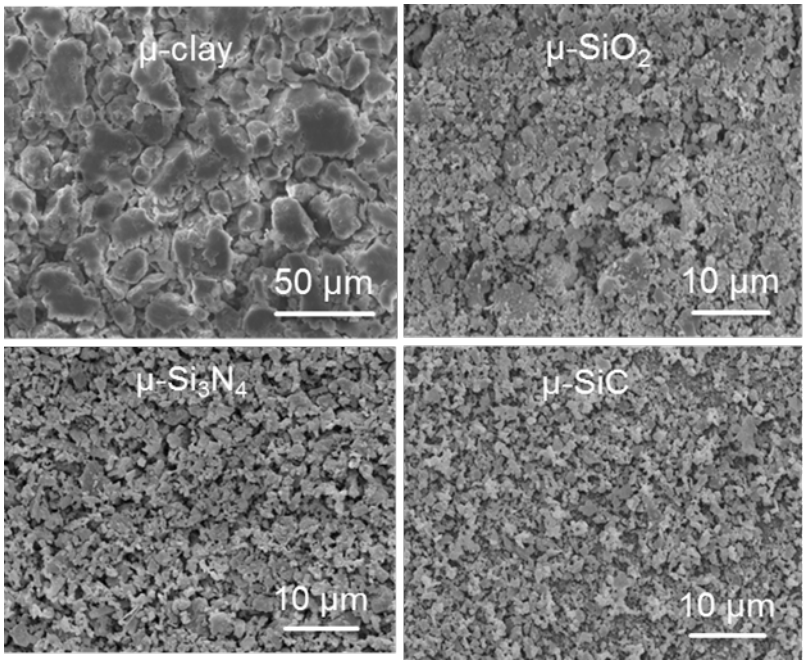
μ-clay
50 μm
μ-SiO2
10 μm
μ-Si3N4
10 μm
μ-SiC
10 μm

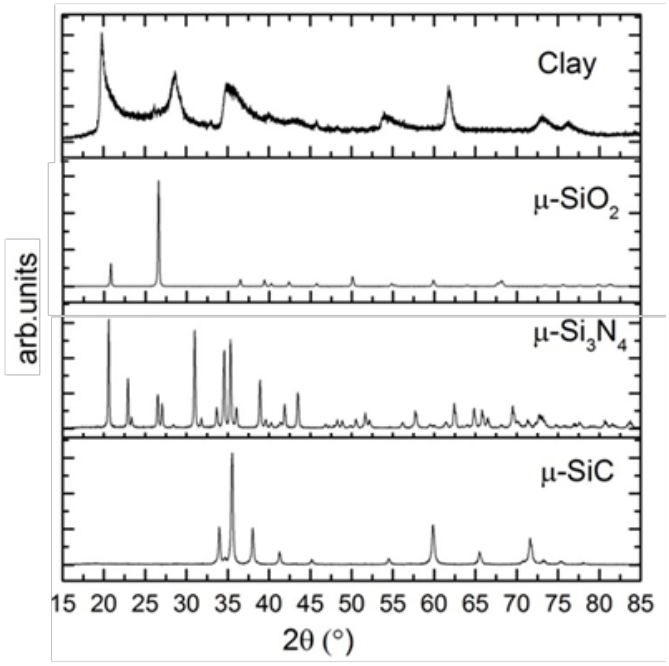
Clay
μ-SiO2
μ-Si3N4
μ-SiC
arb.units
15 20 25 30 35 40 45 50 55 60 65 70 75 80 85
2θ (°)

Fig. 1

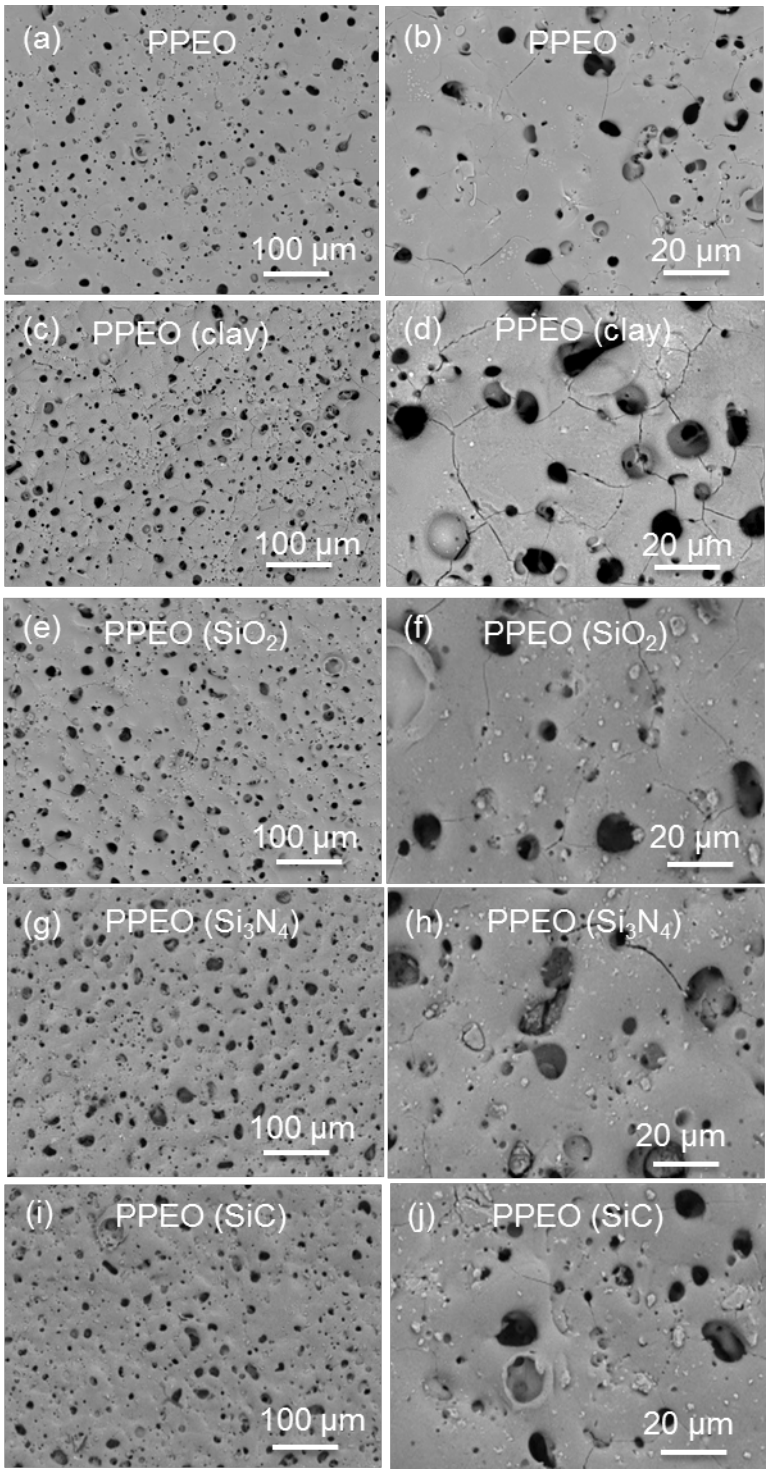
(a) PPEO
100 μm
(b) PPEO
20 μm
(c) PPEO (clay)
100 μm
(d) PPEO (clay)
20 μm
(e) PPEO (SiO_2)
100 μm
(f) PPEO (SiO_2)
20 μm
(g) PPEO (Si_3N_4)
100 μm
(h) PPEO (Si_3N_4)
20 μm
(i) PPEO (SiC)
100 μm
(j) PPEO (SiC)
20 μm

Fig. 2

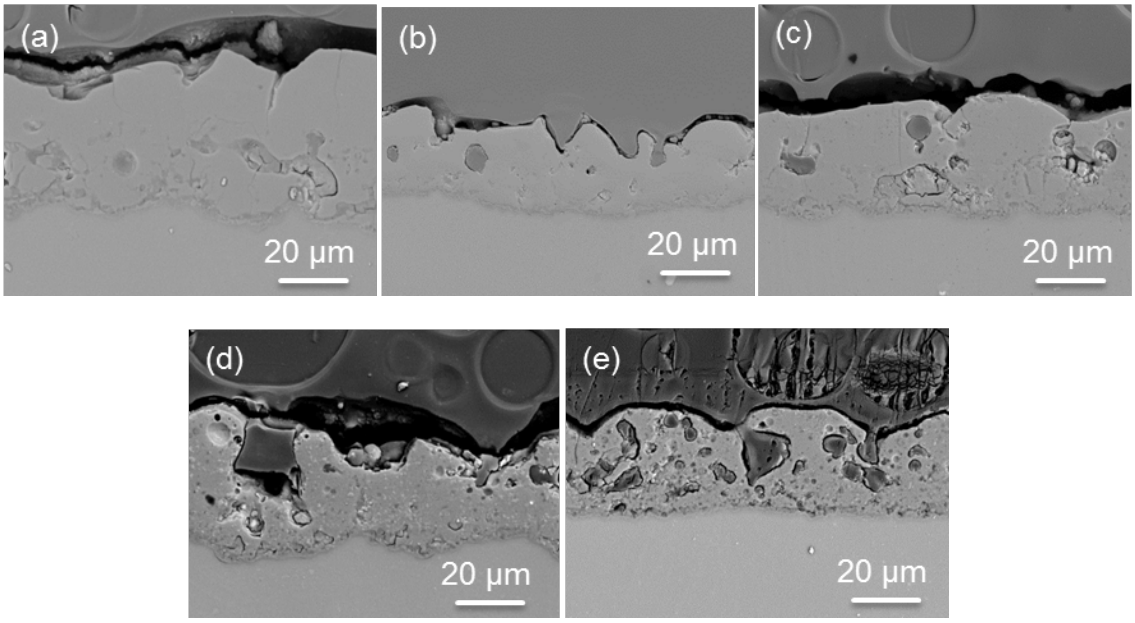

Fig. 3

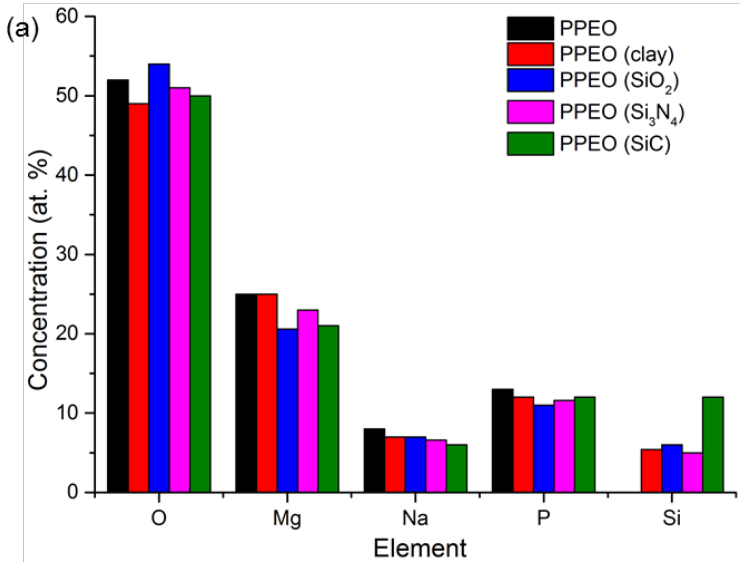
(a)
PPEO
PPEO (clay)
PPEO (SiO2)
PPEO (Si3N4)
PPEO (SiC)
Concentration (at. %)
0
10
20
30
40
50
60
O
Mg
Na
P
Si
Element

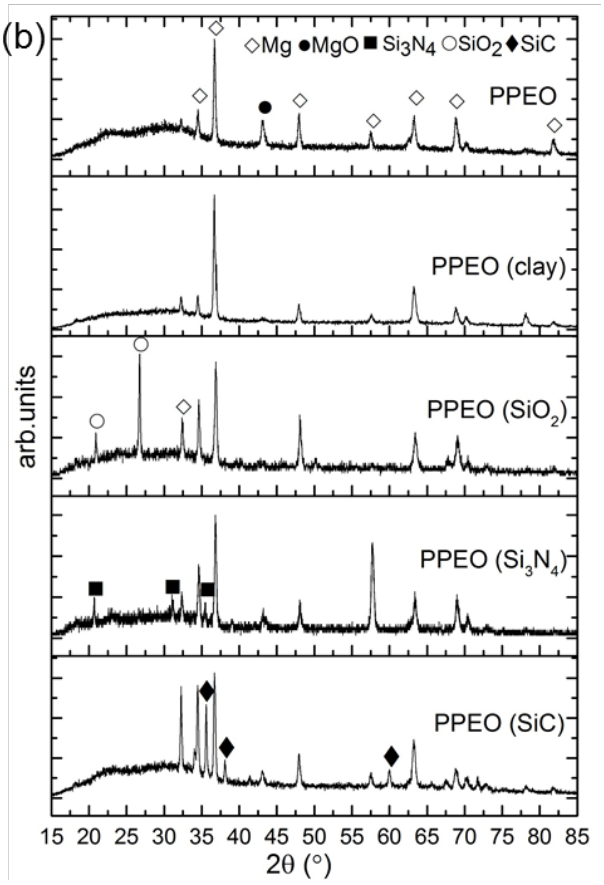
(b)
◇Mg ●MgO ■Si3N4 ○SiO2 ♦SiC
PPEO
PPEO (clay)
PPEO (SiO2)
PPEO (Si3N4)
PPEO (SiC)
arb.units
15 20 25 30 35 40 45 50 55 60 65 70 75 80 85
2θ (°)

Fig. 4

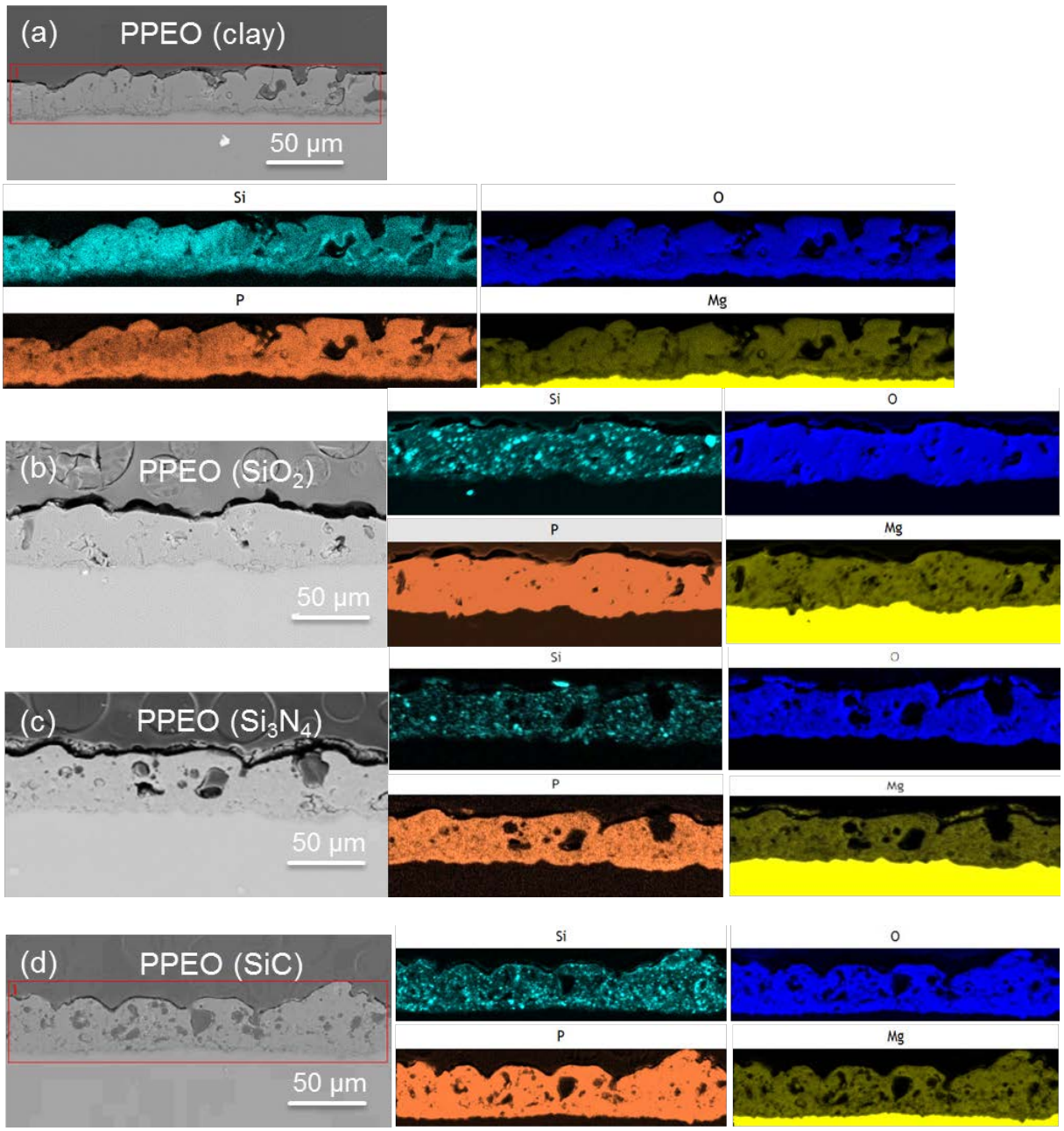
(a) PPEO (clay)
50 μm
Si
O
P
Mg
(b) PPEO (SiO_2)
50 μm
Si
O
P
Mg
(c) PPEO (Si_3N_4)
50 μm
Si
O
P
Mg
(d) PPEO (SiC)
50 μm
Si
O
P
Mg

Fig. 5

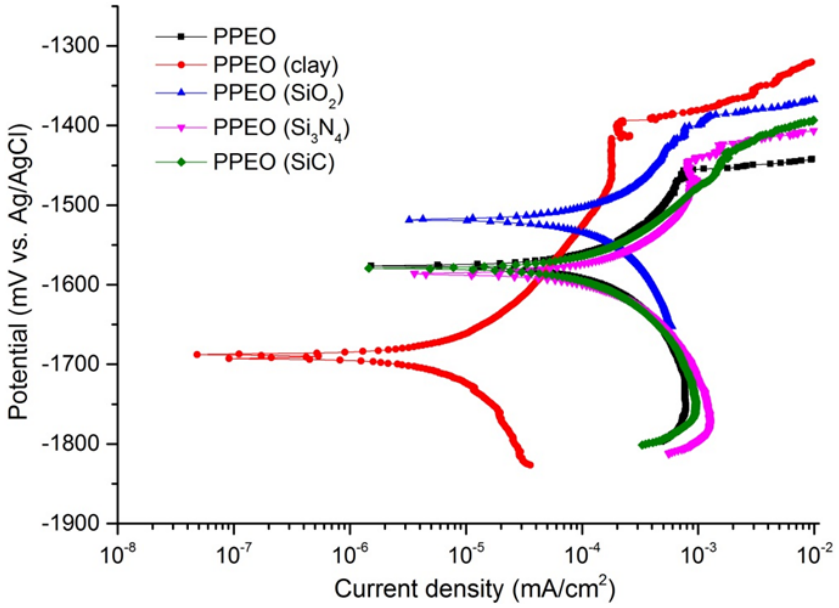
PPEO
PPEO (clay)
PPEO (SiO_2)
PPEO (Si_3N_4)
PPEO (SiC)
Potential (mV vs. Ag/AgCl)
-1300
-1400
-1500
-1600
-1700
-1800
-1900
10^{-8}
10^{-7}
10^{-6}
10^{-5}
10^{-4}
10^{-3}
10^{-2}
Current density (mA/cm^2)

Fig. 6

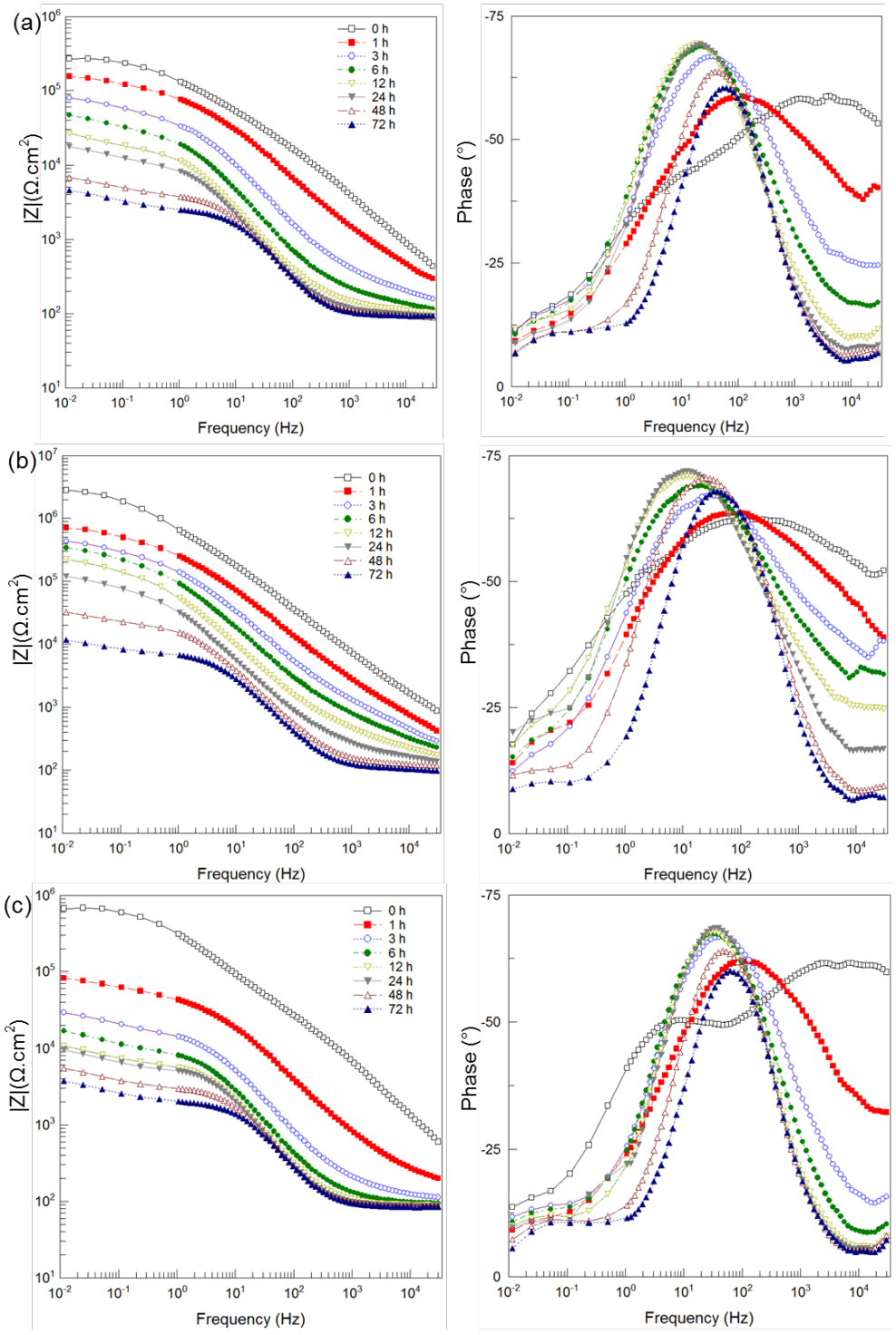
(a)
(b)
(c)
0 h
1 h
3 h
6 h
12 h
24 h
48 h
72 h
|Z|(Ω.cm²)
Phase (°)
Frequency (Hz)

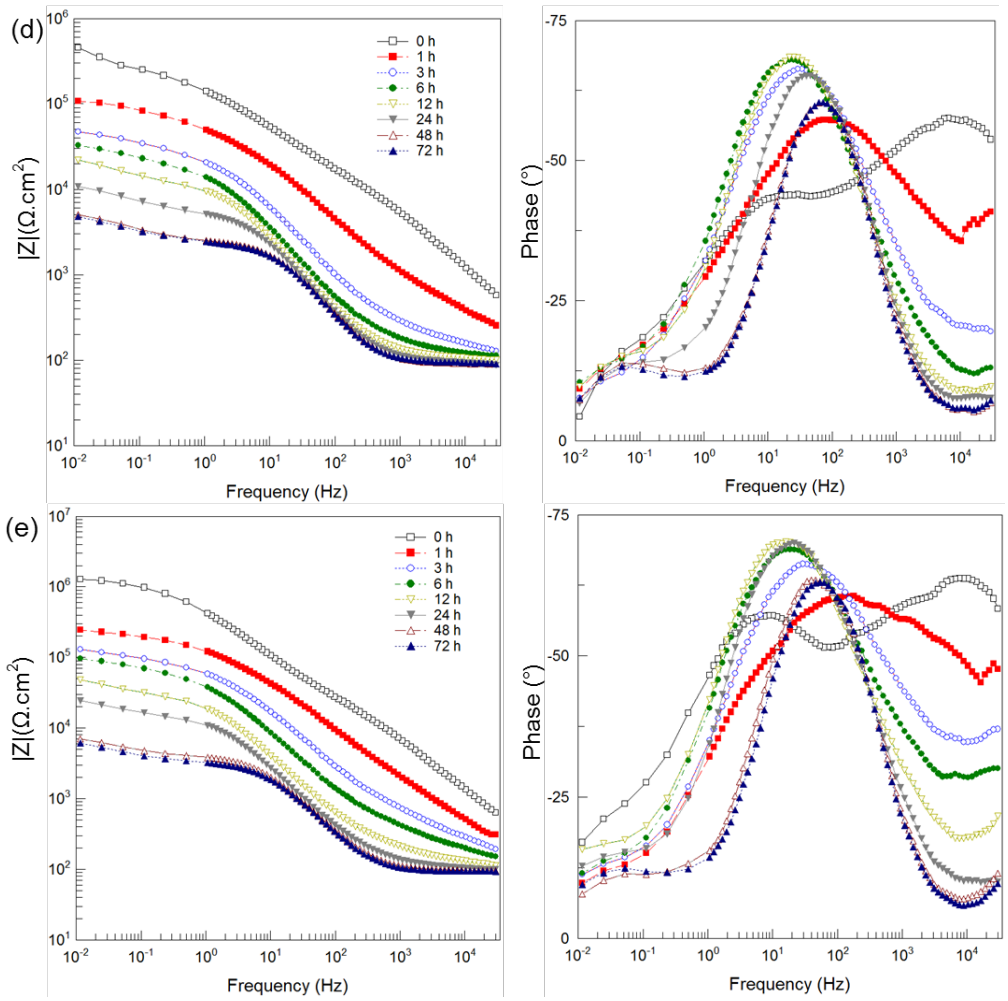
(d)
|Z|(Ω.cm²)
Frequency (Hz)
Phase (°)
Frequency (Hz)
0 h
1 h
3 h
6 h
12 h
24 h
48 h
72 h
(e)
|Z|(Ω.cm²)
Frequency (Hz)
Phase (°)
Frequency (Hz)
0 h
1 h
3 h
6 h
12 h
24 h
48 h
72 h

Fig. 7

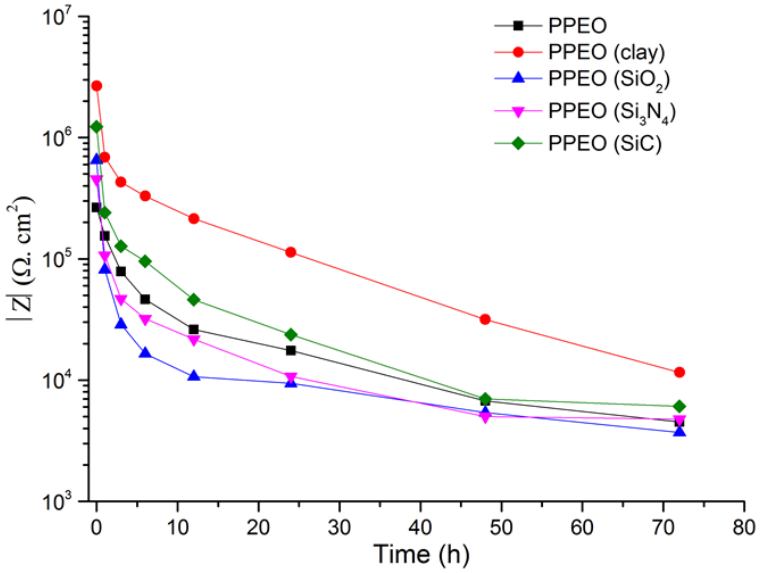
PPEO
PPEO (clay)
PPEO (SiO_2)
PPEO (Si_3N_4)
PPEO (SiC)
|Z| (Ω. cm^2)
10^7
10^6
10^5
10^4
10^3
0
10
20
30
40
50
60
70
80
Time (h)

Fig. 8

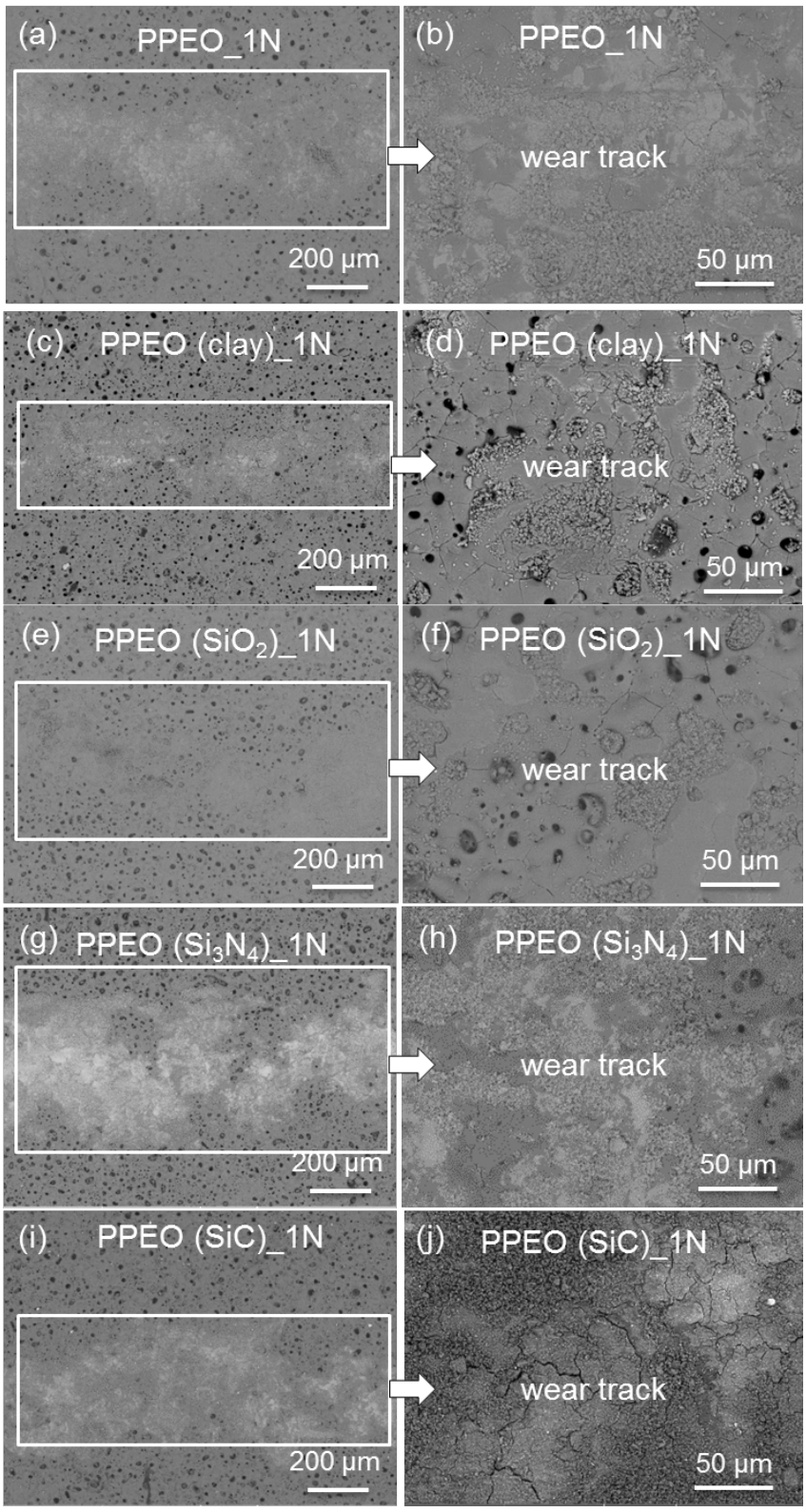
(a) PPEO_1N
200 µm
(b) PPEO_1N
wear track
50 µm
(c) PPEO (clay)_1N
200 µm
(d) PPEO (clay)_1N
wear track
50 µm
(e) PPEO (SiO_2)_1N
200 µm
(f) PPEO (SiO_2)_1N
wear track
50 µm
(g) PPEO (Si_3N_4)_1N
200 µm
(h) PPEO (Si_3N_4)_1N
wear track
50 µm
(i) PPEO (SiC)_1N
200 µm
(j) PPEO (SiC)_1N
wear track
50 µm

Fig. 9

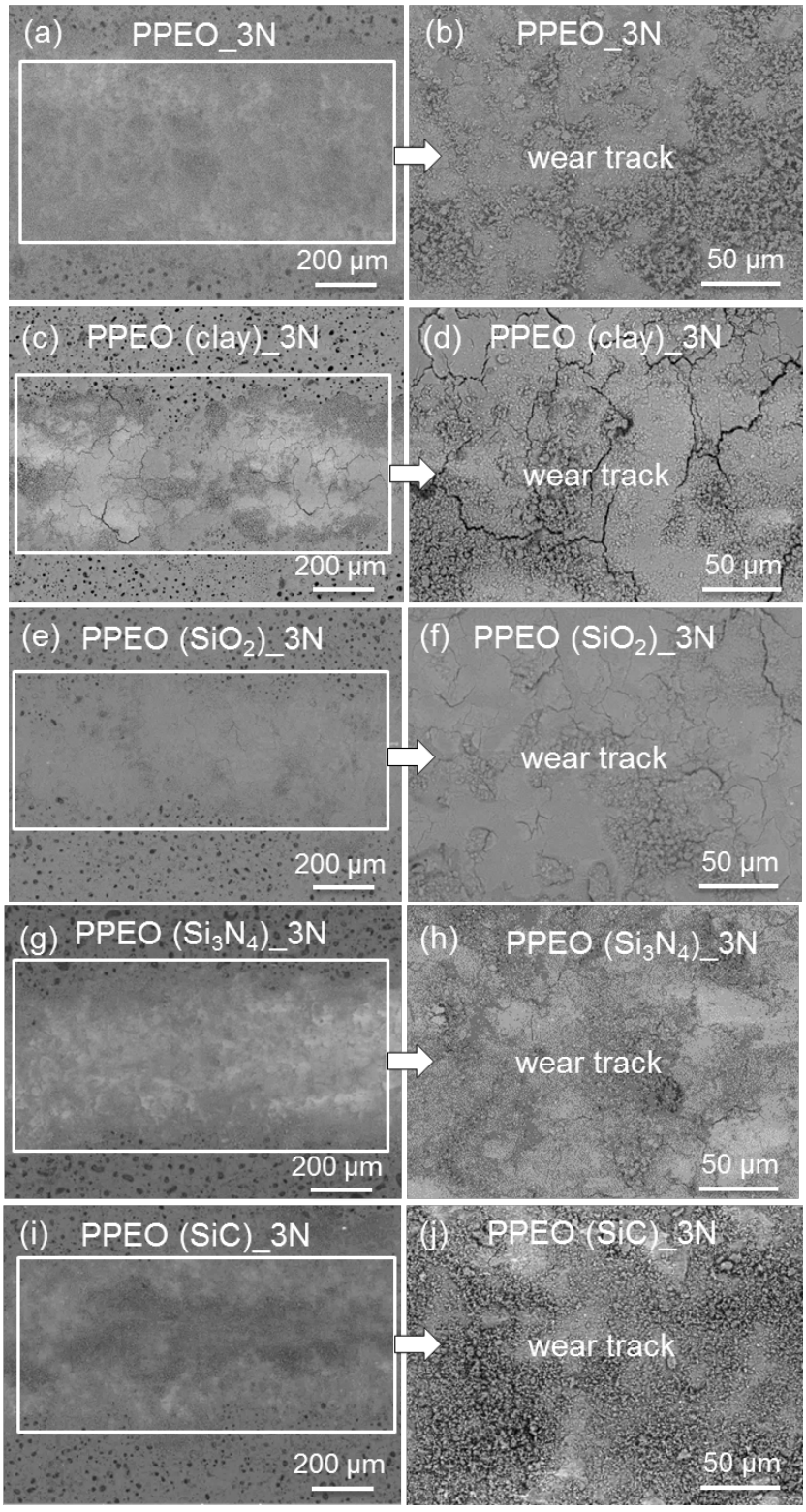
(a) PPEO_3N
200 μm
(b) PPEO_3N
wear track
50 μm
(c) PPEO (clay)_3N
200 μm
(d) PPEO (clay)_3N
wear track
50 μm
(e) PPEO (SiO_2)_3N
200 μm
(f) PPEO (SiO_2)_3N
wear track
50 μm
(g) PPEO (Si_3N_4)_3N
200 μm
(h) PPEO (Si_3N_4)_3N
wear track
50 μm
(i) PPEO (SiC)_3N
200 μm
(j) PPEO (SiC)_3N
wear track
50 μm

Fig. 10

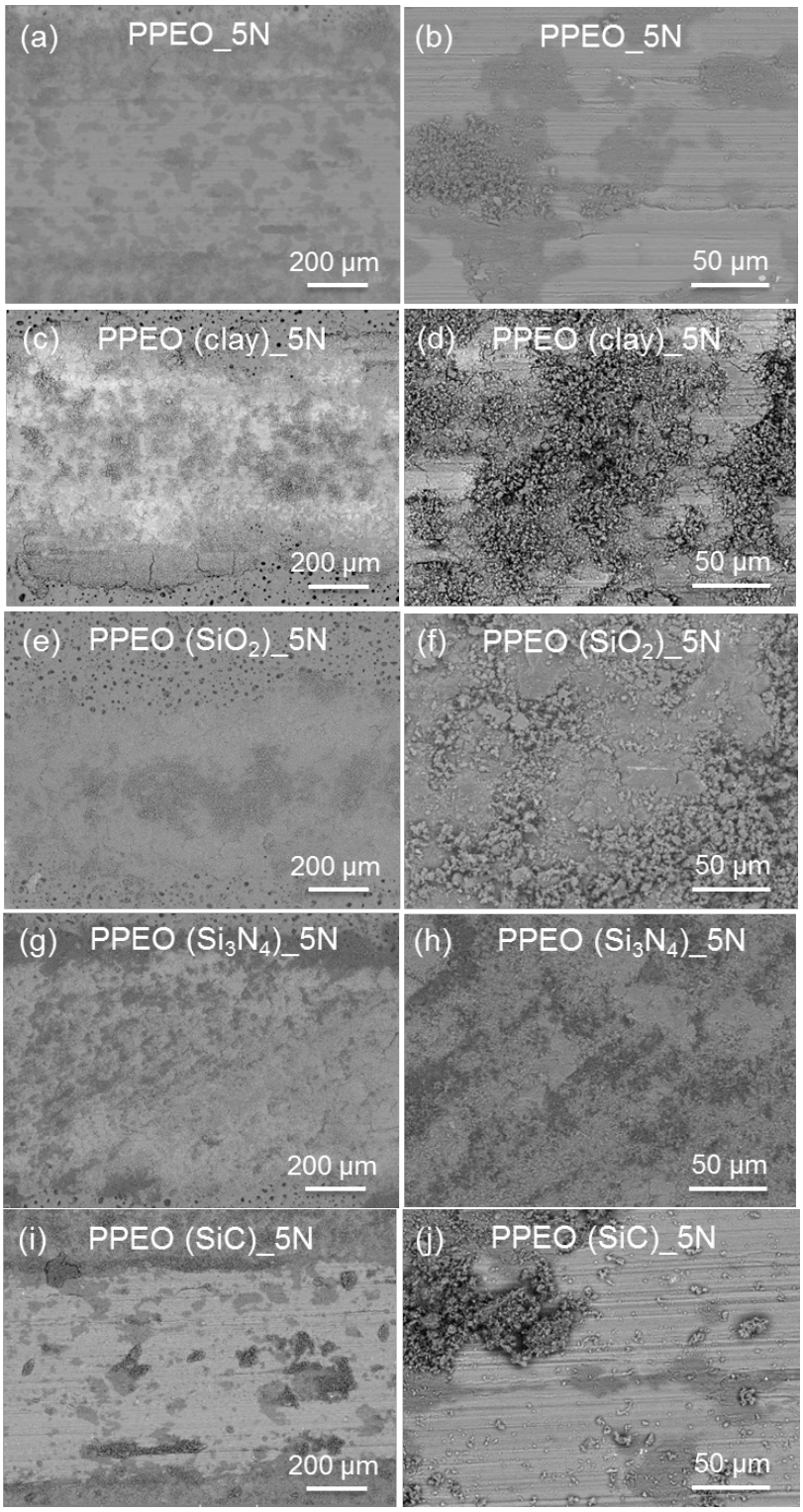
(a) PPEO_5N
200 µm
(b) PPEO_5N
50 µm
(c) PPEO (clay)_5N
200 µm
(d) PPEO (clay)_5N
50 µm
(e) PPEO (SiO_2)_5N
200 µm
(f) PPEO (SiO_2)_5N
50 µm
(g) PPEO (Si_3N_4)_5N
200 µm
(h) PPEO (Si_3N_4)_5N
50 µm
(i) PPEO (SiC)_5N
200 µm
(j) PPEO (SiC)_5N
50 µm

Fig. 11

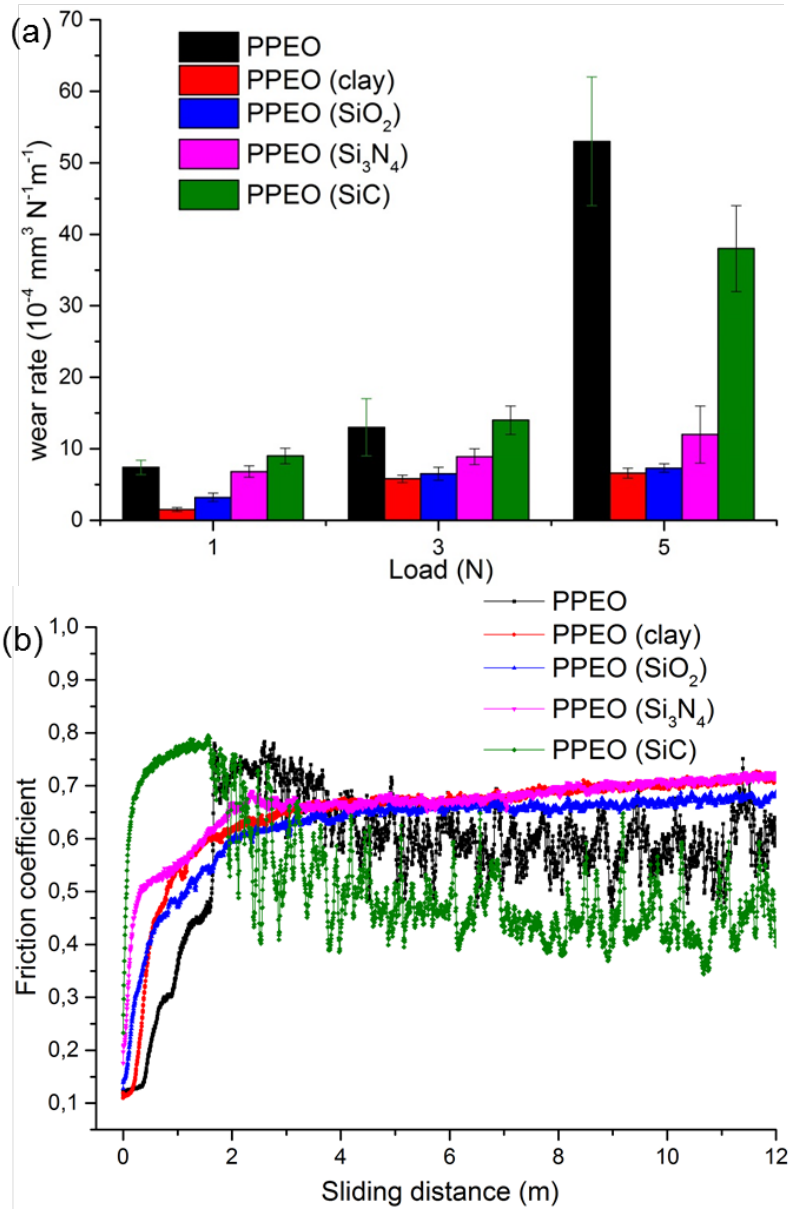
(a)
PPEO
PPEO (clay)
PPEO (SiO2)
PPEO (Si3N4)
PPEO (SiC)
wear rate (10-4 mm3 N-1m-1)
Load (N)
(b)
Friction coefficient
Sliding distance (m)

Fig. 12

Table 1: Electrochemical data of the coatings from polarization test.

Coating	E_{corr} (mV)	i_{corr} (mA/cm^2)	E_{bd} (mV)
PPEO	-1588 ± 10	$(1.2 \pm 0.2)\times10^{-4}$	-1449 ± 8
PPEO (clay)	-1680 ± 8	$(8.7 \pm 2.2)\times10^{-6}$	-1398 ± 8
PPEO (SiO_2)	-1566 ± 36	$(1.9 \pm 0.7)\times10^{-4}$	-1433 ± 6
PPEO (Si_3N_4)	-1578 ± 9	$(1.8 \pm 0.5)\times10^{-4}$	-1466 ± 17
PPEO (SiC)	-1552 ± 7	$(2.0 \pm 0.3)\times10^{-4}$	-1455 ± 10